Experimental Investigation of Droplet Distributions from a Plunging Breaker with Different Wind Conditions

Reyna Guadalupe Ramirez de la Torre[1], Petter Vollestad[1], and Atle Jensen[1]

[1]University of Oslo

November 30, 2022

Abstract

Understanding the droplet cloud and spray dynamics is important on the study of the ocean surface and marine boundary layer. Several of the relevant phenomena depend highly on the characteristics of the spray produced by waves. Nonetheless, the role that the wave energy and the type of wave breaking plays in the resulting distribution and dynamics of droplets is yet to be understood. The aim of this work was to generate violent plunging breakers in the laboratory, quantify the produced droplets, obtaining their sizes and dynamics and to analyze the effect of the different wind speeds on the droplet production. It was found that the mean radius increases with the wave energy and the shape of the initial distribution of droplet sizes does not change with the presence of wind. Also, indications of turbulence affecting the droplet dynamics at wind speeds of 5m/s were found. The amount of large droplets (radius > 1mm) found in this work was larger than expected from the literature. An improved estimation of the initial distribution of large droplets can largely affect the evolution of the Sea Spray Generation Function, and therefore the estimation of energy and mass transport in the marine boundary layer.

Experimental Investigation of Droplet Distributions from a Plunging Breaker with Different Wind Conditions

R.G. Ramirez de la Torre [1], P. Vollestad[1], A. Jensen[1]

[1]University of Oslo

Key Points:

- Initial Droplet Size Distribution
- Focusing Wave Train
- Spray Generation

Corresponding author: R.G. Ramirez de la Torre, `reynar@math.uio.no`

Abstract

Understanding the droplet cloud and spray dynamics is important on the study of the ocean surface and marine boundary layer. Several of the relevant phenomena depend highly on the characteristics of the spray produced by waves. Nonetheless, the role that the wave energy and the type of wave breaking plays in the resulting distribution and dynamics of droplets is yet to be understood. The aim of this work was to generate violent plunging breakers in the laboratory, quantify the produced droplets, obtaining their sizes and dynamics and to analyze the effect of the different wind speeds on the droplet production. It was found that the mean radius increases with the wave energy and the shape of the initial distribution of droplet sizes does not change with the presence of wind. Also, indications of turbulence affecting the droplet dynamics at wind speeds of $5\,\mathrm{ms^{-1}}$ were found. The amount of large droplets (radius $> 1\,\mathrm{mm}$) found in this work was larger than expected from the literature. An improved estimation of the initial distribution of large droplets can largely affect the evolution of the Sea Spray Generation Function, and therefore the estimation of energy and mass transport in the marine boundary layer.

Plain Language Summary

When ocean waves break, a large amount of bubbles and droplets is produced. The created droplets can travel very far distance and very long times depending on their sizes and the wind conditions. These droplets are an important factor for the changes in the weather close to the water surface but also to changes in the global atmosphere. Temperature, humidity, salinity are only some of the examples of the weather conditions that depend on the droplet presence and movement through the atmosphere. In our study, we try to estimate how many droplets detach from the waves when they break and which sizes do they have. We also try to understand the role of wind in these initial instants. We found that the sizes of the produced droplets are larger than presented in previous research. We also found that the presence of wind is not as important as the wave energy in the production of the different sizes. The characteristics of the droplets produced from wave breaking are very important to understand their evolution through time and their transportation through the atmosphere. Further study of these characteristics will help to produce more accurate models to predict changes in the atmosphere.

1 Introduction

At the ocean surface, a large range of complex two phase flow interactions generate aeration in the ocean and aerosol transport through the air. In the present study, we are interested in wave breaking and marine icing processes. For example, in the Arctic environment the droplets produced after wave breaking are transported by the wind and generate thick layers of ice over the surface of ships and structures in short time. These ice-layers represents a life hazard for the inhabitants of these vessels. Field studies and simulations has been used to address this phenomenon (Dehghani, Naterer, & Muzychka, 2016; Dehghani, Muzychka, & Naterer, 2016; Bodaghkhani et al., 2016; Ryerson, 1990; Borisenkov & Pchelko, 1975), but its complexity has shown that a deeper understanding of the droplet generation is necessary. The study of droplet size distribution becomes important to understand the transport through the marine boundary layer and above. Small droplets can be transported over long distances and remain in the atmosphere for several days, while large droplets remain close to the ocean surface and return to the ocean in shorter time scales but still affect the air-sea fluxes of momentum and enthalpy (Veron, 2015).

Some of the relevant articles for this study were Fairall et al. (2009), Stokes et al. (2013) and Veron et al. (2012) which presented experimental results on spray size distributions and Sea Spray Generation Function (SSGF) produced by different setups: wind generated waves, mechanical generated waves with wind, plunging planar jet, etc. More recently Ortiz-Suslow et al. (2016) conducted an experimental study with mechanical waves and winds up to 54 ms^{-1}. The findings of Ortiz-Suslow et al. (2016) showed a similar power law as the proposed before with an important dependence on the wind velocity. Nonetheless, the proportion of large droplets with long residence times increased compared to the previous works (Fairall et al., 2009; Veron, 2015). In the review, Veron (2015), previous findings and emerging consensus on sea spray generation were summarized. Three types of sea spray production processes are thoroughly analyzed: Film, Jet and Spume produced droplets with radius up to 1mm. These types of droplets have long residence times in the air which allows to estimate the spray size dependence on the wind velocities through time. It also summarizes thoroughly the studies over direct and indirect methods to estimate a SSGF. The review closes by pointing out that one of the main issues to study in the future is the large spume droplets (radius larger than 1 mm), their generation mechanism, initial velocity and dynamic behaviour through the airflow. Moreover, the field studies of droplet distribution on vessels showed that the sizes distributions extend to several millimeters (Bodaghkhani et al., 2016; Ryerson, 1990). The present study is an attempt to contribute to the understanding of the large droplets behaviour. In particular the generation mechanism, initial size distribution and the dynamic behaviour through the airflow.

There are several studies of droplet size distribution and SSGF available, probably the most relevant for this study were Mueller and Veron (2009) and Villermaux et al. (2004) where the importance on the initial distribution to estimate the shape of the SSGF was addressed. Villermaux et al. (2004) proposed a Γ-distribution to fit the droplets created after the break-up and coalescence of what they called *ligaments* that detached from the main water bulk. They show the dependence of the droplet distribution on the volume and diameter of these ligaments independently of the shape of the liquid bulk. Then, Mueller and Veron (2009) used the proposed Γ-distribution as the initial distribution to calculate the shape of the SSFG. They found their proposed function implied considerably larger energy fluxes at low and moderate winds. These findings remark the importance of the individual processes of production and suspension of droplets and point towards the complexity of the initial size distributions due to the variety of such processes.

The importance of the dynamics of the droplet generation and transport has also been studied. The description of dispersion and transport of droplets has been done by examining the motion of a single drop and quantifying the influence of the airflow and turbulence over the droplet. Equations for terminal velocities and drag coefficients have been obtained and related to Reynolds numbers (Re), Stokes numbers (St) and the Kolmogorov time scaling (Clift et al., 2005; Andreas et al., 2010; Crowe et al., 2011). But when dealing with large numbers of droplets, it is also important to consider the statistics of the phenomena. In general, particles moving in a fully developed turbulent flow have velocity components that are Gaussian distributed and the speed follows the Maxwell-Boltzman distribution, similarly to the Brownian motion (Pope, 1994). Also, it has been found that the acceleration components has a stretched exponential shape with largely extended tails compared to a Gaussian distribution (La Porta et al., 2001). This is a phenomenological function for flows with $200 \leq R_\lambda \leq 970$, where R_λ is the Taylor microscale Reynolds number defined in terms of Reynolds number Re as $R_\lambda = (15Re)^{1/2}$. This function has been experimentally confirmed by different articles through out different fluid dynamics applications (Voth et al., 2001; Mordant et al., 2004; Shnapp et al., 2019; Kim & Chamorro, 2019).

In this study we present experimental results for medium and large droplets ($0.15\,\mathrm{mm} \leq r \leq 5.5\,\mathrm{mm}$) generated by plunging breakers. We consider cases without wind and with the presence of low wind (<7 ms^{-1}). The results are compared to previous theoretical and experimental findings. Our work is structured as follows. In section 2, the experimental setup is presented thoroughly. First, the generation of wind and its resultant profiles are detailed. Then, the generation of the focusing wave train and its development in the

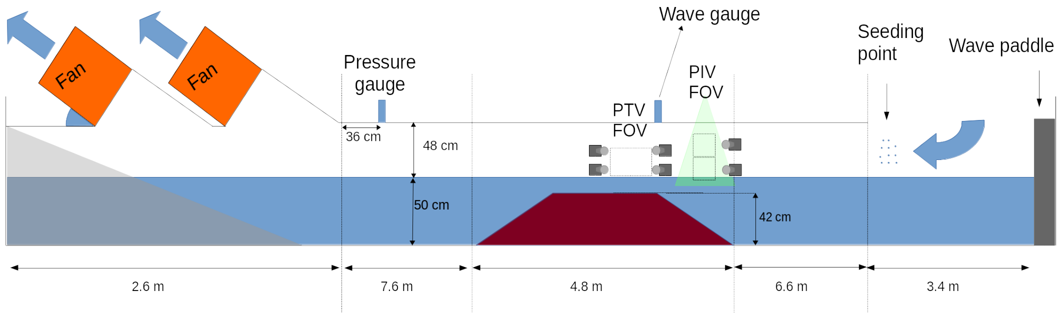

Figure 1. Schematic drawing of the wave tank in the Hydrodynamics Laboratory where the experiments were developed

presence of a beach and wind are presented. In section 3, we present the resultant trajectories and sizes obtained by the use of Three Dimensional Particle Tracking Velocimetry (3DPTV), these results are further analyzed to obtain statistical distributions of initial droplet diameter, vertical reach, velocity and accelerations. Each of this statistical analysis are related to relevant theoretical and experimental findings.

2 Experimental Methods

The experiments were conducted in the Hydrodynamics Laboratory at the University of Oslo, in the wave tank with dimensions $25 \times 0.52 \times 1\,\mathrm{m}$ where the mean water level for all experiments was $0.5\,\mathrm{m}$. In this work violent plunging breakers are made and the produced droplets are quantified, obtaining their sizes and dynamics and analyzing the effect of the different wind speeds on the droplet production. The experiment consisted of three main measuring techniques: the generation and analysis of a focusing wave train that steepens by the effects of a slope, the wind velocity profiles produced on top of the waves and the detection of the droplet cloud created after the break. Hereafter, the different analysis tools are described in detail.

2.1 Wind Profiles

The wind profiles, without the influence of mechanically generated waves, were measured using particle image velocimetry (PIV). The center of the field of view (FOV) is 10.75 meters from the wave paddle in the location "PIV FOV", indicated in figure 1. Two Photron WX100 (2048x2048 pixels) cameras with 50 mm lenses are used, each providing a FOV of approximately 18x18 cm. The cameras were positioned in a vertical arrangement, as indicated in figure 1. The air phase was seeded with small ($\approx 6\ \mu m$) water droplets generated from a high pressure atomizer. The centerplane was illuminated by a 147 mJ ND:YAG double pulsed laser. The cameras were set to acquire images at a rate of 30 fps, and a frame straddling technique was employed to control the effective Δt between an image pairs used for PIV. Hence, 15 velocity fields were acquired per second. Δt was varied between 150 and 350 μs depending on the air velocity in the flume. The images (800 per experimental case) were processed in Digiflow by Dalziel Research partners (Dalziel, 2017), with a final subwindow size of 80x80 pixels, and 50 % overlap.

The lower part of the velocity profiles (some distance above the waves) were found to be well represented by a logarithmic velocity profile:

$$u = \frac{u_*}{\kappa} \ln(y/y_0), \tag{1}$$

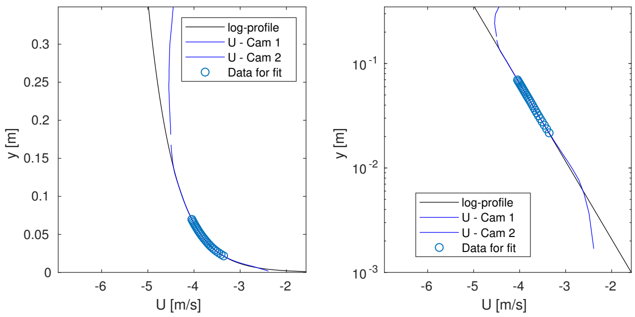

Figure 2. Example recorded velocity profile (blue lines), data points used for fit with equation 1 (blue circles) and resulting log-profile (black line). Illustrated with linear (left) and semilogarithmic (right) axis.

where u_* is the wind friction velocity, κ is the Von Karman constant (set equal to 0.41) and y_0 is the roughness height. Equation 1 was fitted to a part of the velocity profile exhibiting a logarithmic profile, deducing u_* and y_0, as shown in figure 2. The logarithmic profile was then used to estimate an equivalent U_{10} (mean velocity evaluated 10 meters above the surface). Results are presented in table 1, together with the peak horizontal velocity recorded (U_{max}).

Table 1. Results from the wind profile analysis.

Wind case	U_{max} [m/s]	u_* [m/s]	y_0 [mm]	U_{10} [m/s]
1	3.41	0.151	0.0185	5.14
2	3.91	0.201	0.0403	6.09
3	5.09	0.286	0.0984	8.03
4	5.45	0.308	0.1015	8.64
5	6.16	0.341	0.0864	9.70

2.2 Generation of Focusing Wave Trains

The mechanically generated waves were made by a horizontal displacement wave paddle, shown in figure 1. To modify the wave energy, different wave amplitudes were generated by varying the maximum voltage input V_m, the maximum amplitude a_{max} for each V_m is shown in table 2. A group of focusing waves is created using this input voltage time history (Brown & Jensen, 2001):

$$V(t) = b(t)\sin\Phi(t) \tag{2}$$

for $0 \leq t \leq t_s$ with

$$b(t) = \frac{256}{27}\frac{t^3(t_s - t)}{t_s^4}V_m \tag{3}$$

$$\Phi(t) = 2\pi f_0 t\left(1 - \alpha\frac{t}{t_s}\right) \tag{4}$$

where the instantaneous wave frequency is approximately

$$\omega(t) = \frac{d\Phi}{dt} = 2\pi f_0\left(1 - 2\alpha\frac{t}{t_s}\right) \tag{5}$$

Table 2. Maximum wave amplitude for the envelope at the focal point x_f, for the different voltage inputs in the wave paddle and maximum steepness ak considering all wave trains have $k = 7.59$ rad/m

V_m [V]	a_{max} [m]	ak
0.4	0.062	0.47
0.5	0.075	0.57
0.6	0.087	0.66

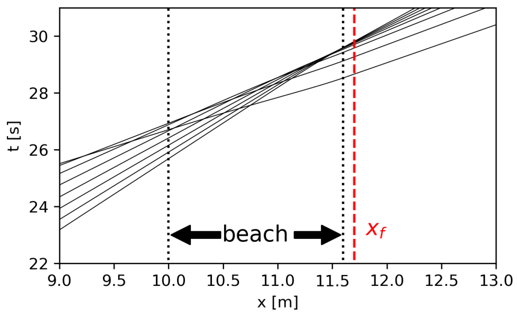

Figure 3. Phase space of focusing wave train, the beach position is limited by the dotted line and the position of the original focusing point x_f is shown with the red line.

Under deep water conditions, $\omega(t)$ produces a perfect focus at

$$x_f = \frac{gt_s}{8\pi\alpha f_0} \tag{6}$$

therefore, to define x_f, the parameters α, t_s and f_0 should be constant. In these experiments, the focal point was defined at $x_f = 11.69\,\text{m}$, approximately the edge of the sloping beach. It is important to notice that the wave number k is only dependent of $\omega(t)$, therefore all cases have defined $k = 7.59$ rad/m at the breaking point, calculated by the dispersion relation for gravity waves.

It was expected that the presence of the beach affected the focus position as the deep water condition became invalid. By looking at the phase space in figure 3, the effects of the sloping beach on the focal point can be predicted. This diagram shows that some of the frequencies will reach x_f faster due to the presence of the beach. Nonetheless, most of the frequencies preserve the original x_f. Furthermore, by comparing the surface elevation at x_f for the wave groups with and without beach (figure 4), it is visible that the caustic or envelope suffers small modifications in the different cases. The solid line shows the no-beach case and the dashed lines show cases with the beach and different wave maker input V_m. All the cases preserve a central and higher component which generates the studied violent breakers. When producing the different wave trains, it is possible to quantify the energy content of the wave group by means of the Fourier transform and the calculation of the mean power $R(0) = \int S(\omega)d\omega$. Figure 4(right) shows the power spectrum of the wave groups at x_f for the different cases. It is obvious that all the cases have the same peak frequency, but the beach cases shows evidence of energy dispersion, which was expected. Over all, the presence of the beach affects the energy and frequency of the group but not the position of the breaking point.

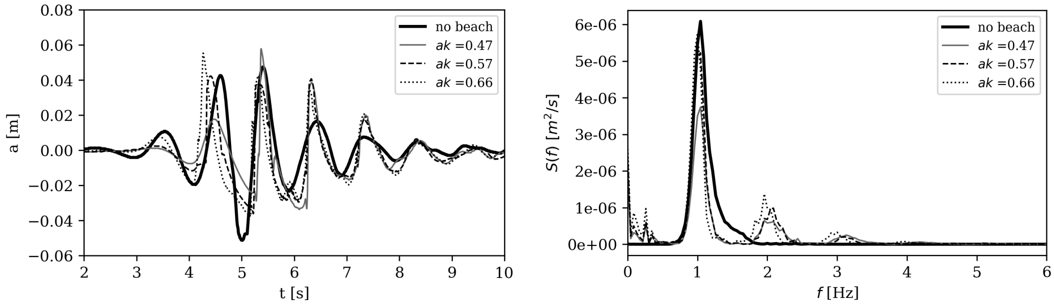

Figure 4. Surface elevation at the focal point for cases with no wind. Power Spectrum of the same cases

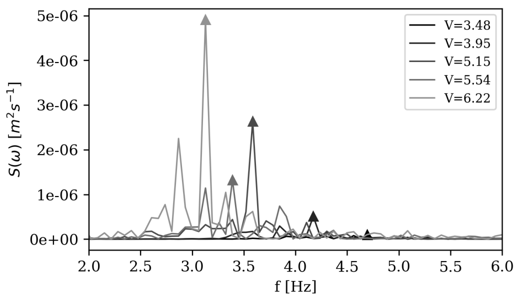

Figure 5. Power spectrum of the wind waves field without the presence of mechanically generated waves

2.3 Wind Generated Waves and their Influence in the Focusing Wave Train

When introducing wind in the air phase, it was expected to obtain a field of wind generated waves. Their characteristics will depend on the wind velocity U_{max} and the fetch, as has been studied in wave theory. The wind wave field will disturb the focusing packet and modify the frequencies and the energy present at the impact. Therefore it was important to quantify the influence of this field in the impact zone. Using the wave gauges, one minute time series of the surface elevation were taken for different wind speeds U_{max} without the presence of the focused packet. The Fast Fourier transform of these series is presented in figure 5. The spectra show that the peak frequency of the wave filed changes with the wind speed. For larger wind speed, the peak frequency decreases and the energy content increases. These frequencies are higher than those for the mechanical generated waves and the magnitude of the coefficients is at most of the same order. From these results, it can be predicted that the influence of the wind wave field will have a minor influence over the mechanical waves.

Figure 6 shows the surface elevation and the frequency spectra for the cases with wind compared to the no-wind and no-beach cases for the maximum steepness ak. Both graphs show similar results to figure 4, the envelope shape has small changes and we can see a slight phase change for the highest components when wind is applied. The frequency domain is also similar to the previous case, with the same peak frequency and some energy dispersion for the wind cases. In conclusion, the beach and wind presence affects the energy content of the wave group and therefore the energy of the breaker. Figure 7 shows the calculated mean power $R(0)$ compared to the different maximum wave steepness: ak and wind velocities: U_{max} used for this work. For the case of $ak = 0.47$ with

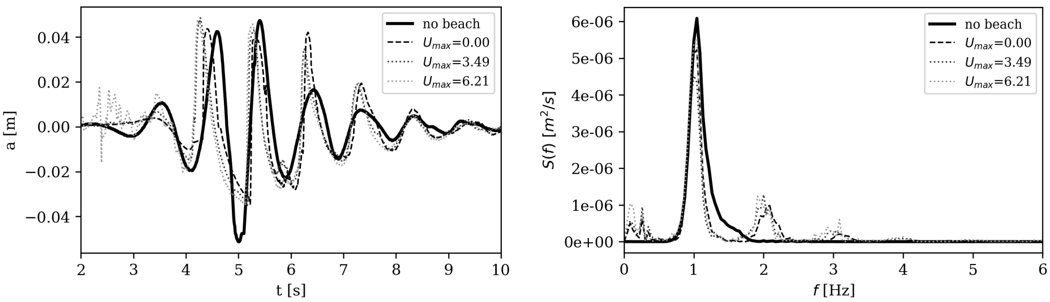

Figure 6. Surface elevation at the focal point for cases with wind. Power Spectrum of the same cases

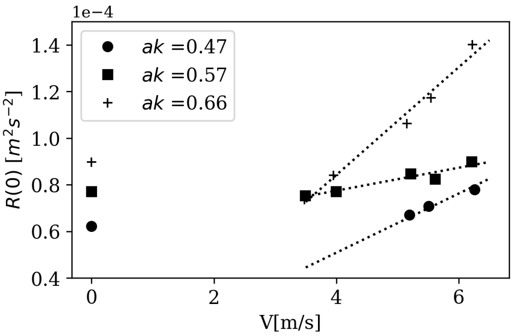

Figure 7. Mean power of the wave series against wind velocity. The different markers represents different wave amplitudes.

wind velocities $U_{max} < 4.5\,\mathrm{ms}^{-1}$ do not generate a plunging breaker, therefore this data is not accounted in the study. The estimated energy will be compared to the results of the droplet clouds.

2.4 3DPTV

After the breaker, a cloud of droplets is generated by the impact. The trajectories of the droplets are followed using 3DPTV. Images of the cloud are taken by 4 Monochromatic AOS Promon cameras with 50mm lenses. The frame rate is 167 fps and the image resolution is 1920×1080pixels. The FOV right side is located on the breaking point to obtain all the splashing occurred in front of the wave, as shown in figure 1. The three-dimensional FOV is approximately $0.25 \times 0.15 \times 0.20\,\mathrm{m}$, as shown in Figure 8. A sequence of 2 seconds during and after the breaking is recorded. The 4-camera system is used to obtain the 3D positions and trajectories using the open source software OpenPTV (Consortium et al., 2012). From the post processing we can also obtain size distributions of the droplet cloud. A set of 5 repetitions was developed for each wave amplitude and wind speed.

The breaking and spray generation process happens in a span of less than one second, and the physical event has an inherent randomness. Therefore the results of the 5 experiments are used as an ensemble in the statistics. For each droplet we collect their size, position, velocity and acceleration in each time step. Every time step is also consider in the analysis. As it was expected, we observed the droplets are not always spherical and their deformation increases with the size. The equivalent diameter D_e is com-

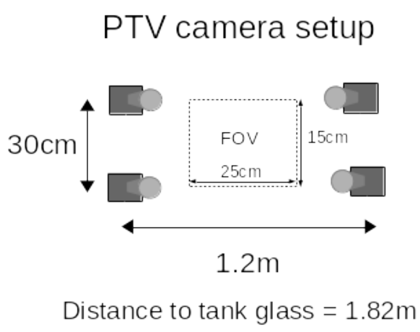

Figure 8. Schematic drawing of the 4-camera setup for 3DPTV

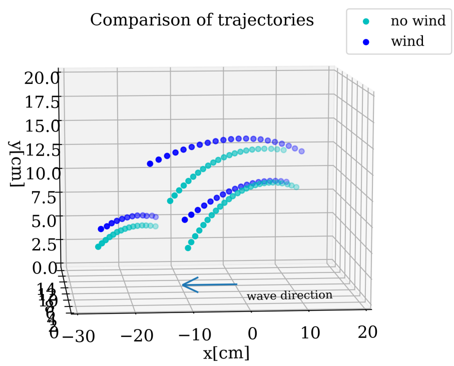

Figure 9. Examples of the trajectories obtained

Table 3. Total number of droplets analyzed

	$U_{max} = 0\,\mathrm{ms^{-1}}$	$U_{max} = 5.2\,\mathrm{ms^{-1}}$	$U_{max} = 6.2\,\mathrm{ms^{-1}}$
$ak = 0.47$	1518	10455	17310
$ak = 0.57$	8046	11001	10650
$ak = 0.66$	9154	13292	12272

monly used to classify droplet sizes with one unique parameter and is commonly defined as $D_e = \sqrt{ab}$, where a and b are the major and minor axis of the ellipsoid. In addition, to calculate the values of a and b we use an averaged value from the 4 images obtain by the camera array.

3 Results and Discussion

A sample of 3D trajectories are presented in Figure 9, the trajectories have parabolic shape as expected, but with the increasing wind the shape tends to be more skewed. The total number of analyzed particles can be found in Table 3. In general, the number of droplets produced in the impact grows with the wind conditions. No clear trend is visible with the steepness of the wave. This might be a consequence of the different breaking presented on each case. Figure 10 shows the equivalent diameter D_e and height distributions of droplets for different cases, the vertical panels shows different wind speeds

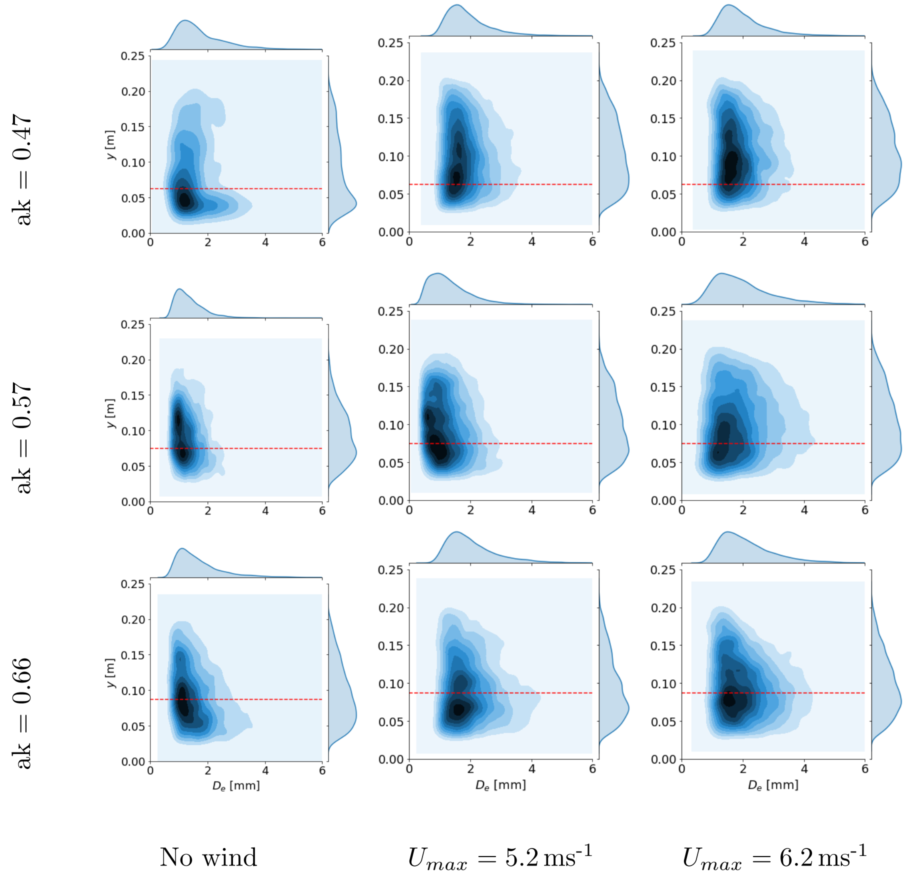

Figure 10. Equivalent Diameter D_e distribution versus height distribution for the different steepness ak and wind velocities U_{max}. The red dotted line represents the maximum wave height before breaking.

U_{max} and the different horizontal panels show different wave steepness ak. The maximum wave amplitude a_{max} is depicted with a red line. In all cases, higher concentrations of larger particles are presented when the wind is applied. When $U_{max} = 0$ the particles with $D_e > 2mm$ are clearly found only under a_{max}. In contrast, larger concentrations of these particles are found over a_{max} for the wind cases. This result agrees with the hypothesis that more droplets will be transported further by the wind. When $ak = 0.57$ the presence of large droplets is small compared to the other cases, this might be a consequence of a different type of breaking. By visual inspection, the amount of spray is visibly different, although a violent breaking is present in all cases. But it is difficult to quantify the difference in the breaking process.

Figure 11 shows the Probability Distribution for D_e, the solid lines correspond to the Γ-distributions as proposed by Villermaux et al. (2004):

$$\Gamma(x; n) = \frac{n^n x^{n-1} e^{-nx}}{\Gamma(n)} \tag{7}$$

where n^{-1} is the variance and $x = D_e/\overline{D_e}$ is the diameter normalized by the mean. Values of n lie between 3.5 and 7 and are similar to those in Villermaux et al. (2004). Another relation proposed by Villermaux et al. (2004) was between n and the ratio $\overline{D_e}/\xi$,

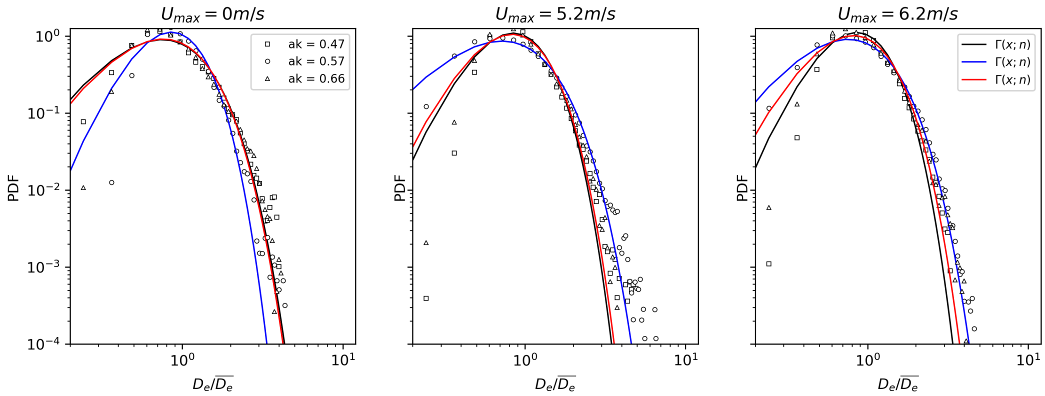

Figure 11. Probability Distribution of D_e compared to distribution proposed by Villermaux et al. (2004)and used in Mueller and Veron (2009)

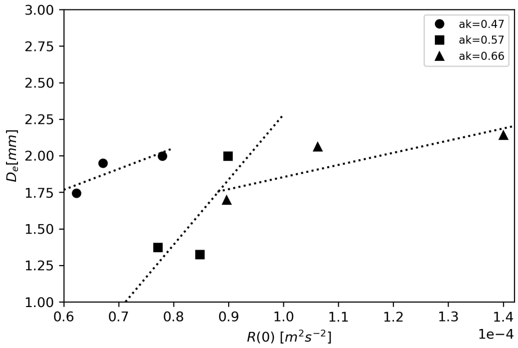

Figure 12. Mean power of the wave series against mean equivalent diameter.

where ξ is the average diameter of a ligament. In a general, this relation can be expressed as:

$$N\frac{\overline{D_e}}{\xi} \simeq e^{\frac{n}{3}} \tag{8}$$

with N being a normalization factor that depends on the initial length of the ligament. Mueller and Veron (2009) presents the simplified relation: $n = 0.4(\overline{D_e}/\xi) + 2$. In contrast, for this investigation, the relation has the shape: $n = 12.34(\overline{D_e}/\xi) - 2$.

Figure 12 shows $\overline{D_e}$ for the different cases. From the figure, it is observed that $\overline{D_e}$ increases with $R(0)$ of the wave. According to Mueller and Veron (2009): $D_0 \approx 2.5D_e$, where D_0 is the diameter of a sphere with the equivalent volume as the average ligament, this means that the water volume contained in a ligament increases with the energy of the impact. Previously, it has been found that the mean size of droplets decreases with the presence of high winds (Mueller & Veron, 2009; Ortiz-Suslow et al., 2016; Fairall et al., 2009). Our findings suggest that it is the break-up of larger droplets in the turbulent flows that contributes to the generation of smaller droplets. Therefore the study of large droplets breakup in high wind could be of interest.

3.1 Velocity Distributions

Figure 13 shows the probability distributions of the velocity components for all the droplets analyzed in the different cases. The vertical panels show the different U_{max} and

Table 4. Mean of velocity components by U_{max} and velocity component

	$U_{max} = 0\,\mathrm{ms^{-1}}$	$U_{max} = 5.2\,\mathrm{ms^{-1}}$	$U_{max} = 6.2\,\mathrm{ms^{-1}}$
u	0.29 m/s	0.14 m/s	0.29 m/s
v	0.20 m/s	0.17 m/s	0.20 m/s
w	0.00 m/s	0.00 m/s	0.00 m/s

the horizontal panels show the different velocity components. The different ak are shown with distinct markers and a solid line shows the Gaussian distribution with the same mean and standard deviation as the data. The similarity with the Gaussian distribution increases for wind cases. The mean value is different for each component, but consistent through the same U_{max} and independent of ak as shown in table 4. When $U_{max} = 0$ the probability for droplets with the mean velocity is larger than the estimated by the Gaussian distribution, especially in the u and w components which refer to the horizontal components. On the other hand, v the vertical component presents a larger probability for extreme cases when there is no wind. This means that the largest vertical velocity is dampened by the presence of wind. For all components, the standard deviation increases with U_{max}, which is more likely by an indication of the forcing applied on the droplets by the wind, the forcing increases the variability of the instantaneous velocities in each droplets, creating larger deviations from the mean.

From the velocity components, the speed $|\overline{u}|$ can be calculated and the distributions obtained are presented in Figure 14. The different ak are represented by different markers and the solid line represents the Maxwell-Boltzman(*M-B*) distribution with the same mean value. *M-B* distribution represents the speed of particles moving in three dimensions with Gaussian distributed velocity components. The top graphs show the distribution for $U_{max} = 0$ and the bottom graphs summarizes the results for the other cases. In general, is visible that the speed distributions for $U_{max} = 0$ are dependent on the values of ak and differs largely from the *M-B* distribution, while the other cases become independent of ak and follow closely the *M-B* distribution. When there is no wind, the data distributions present larger probability for extreme values, both towards zero and the maximum speed. This is probably related to the fact that the velocity components do not present a Gaussian shape. On the other hand, when wind is introduced, the speed distribution resembles closely the *M-B* distribution, therefore we can confirm the components of the velocity have Gaussian behaviour. Physically, this is a significant finding, because the Gaussian and *M-B* distributions of the velocity are related to random and turbulent processes which are expected when wind is introduced. The large differences for cases without wind are probably a consequence of the parabolic trajectories where the velocity components are statistically dependent.

3.2 Acceleration Distributions

Figure 15 shows the probability distribution of the acceleration components normalized by their standard deviation $a_i/ < a_i^2 >^{1/2}$ in the wind direction a_x and in the vertical direction a_y. The different ak are shown with different markers and the vertical panels shows different cases of U_{max}. The dashed line represents the Gaussian distribution with the same standard deviation and the solid line shows the exponential distribution proposed by La Porta et al. (2001) and defined by:

$$C \exp\left(-\frac{a^2}{(1 + |a\beta/\sigma|^\gamma)\sigma^2}\right) \tag{9}$$

with $\beta = 0.539$, $\sigma = 0.508$, $\gamma = 1.588$, for the results presented here the constant $C = 0.67$. In all cases the probability for extreme cases is larger than the expected in

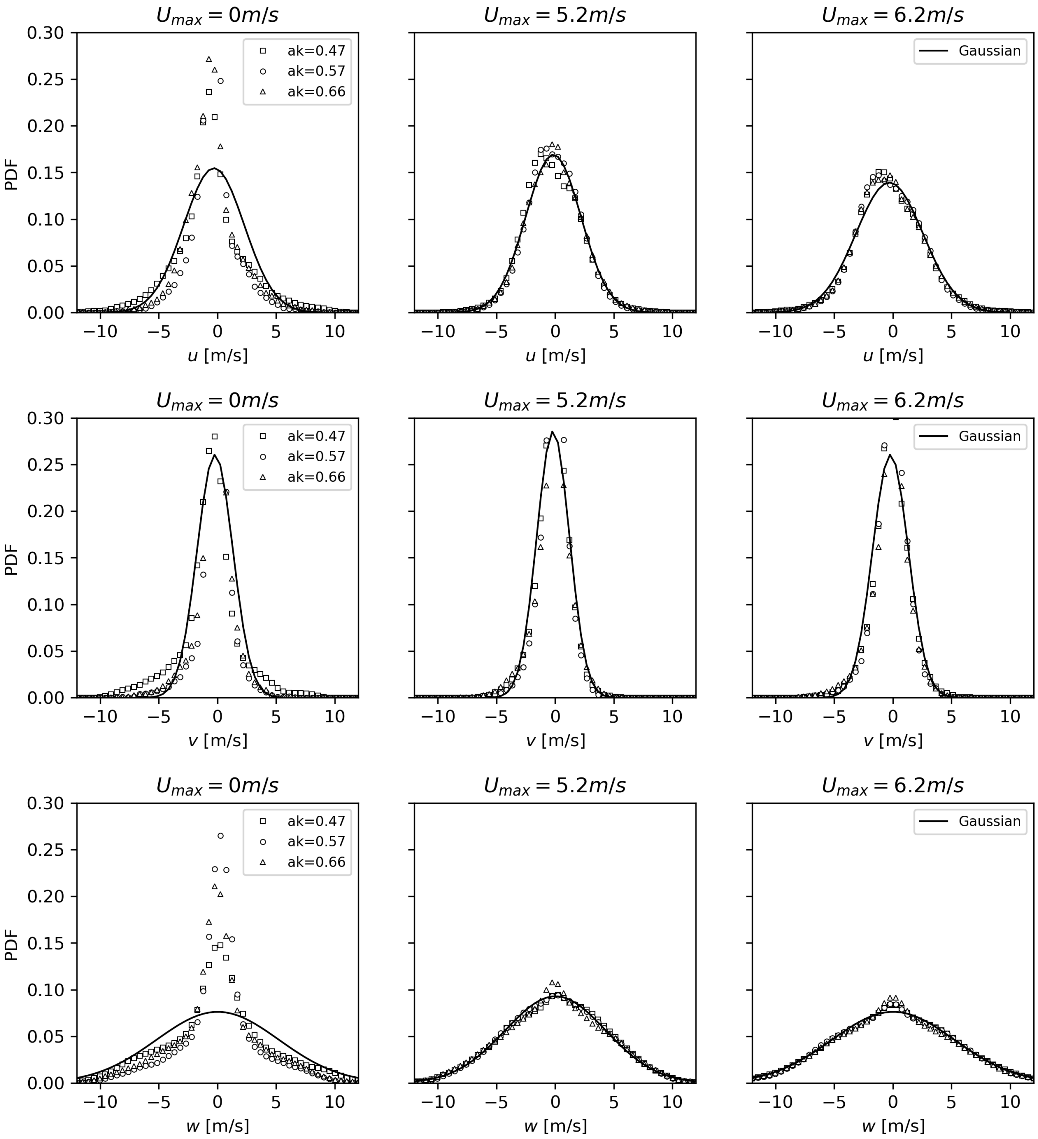

Figure 13. Probability distribution for the different velocity components for the different wind cases. Maximum values of Re are $Re_0 = 120$, $Re_{5.2} = 5500$ and $Re_{6.2} = 6500$; where the subscript refers to the correspondent U_{max}

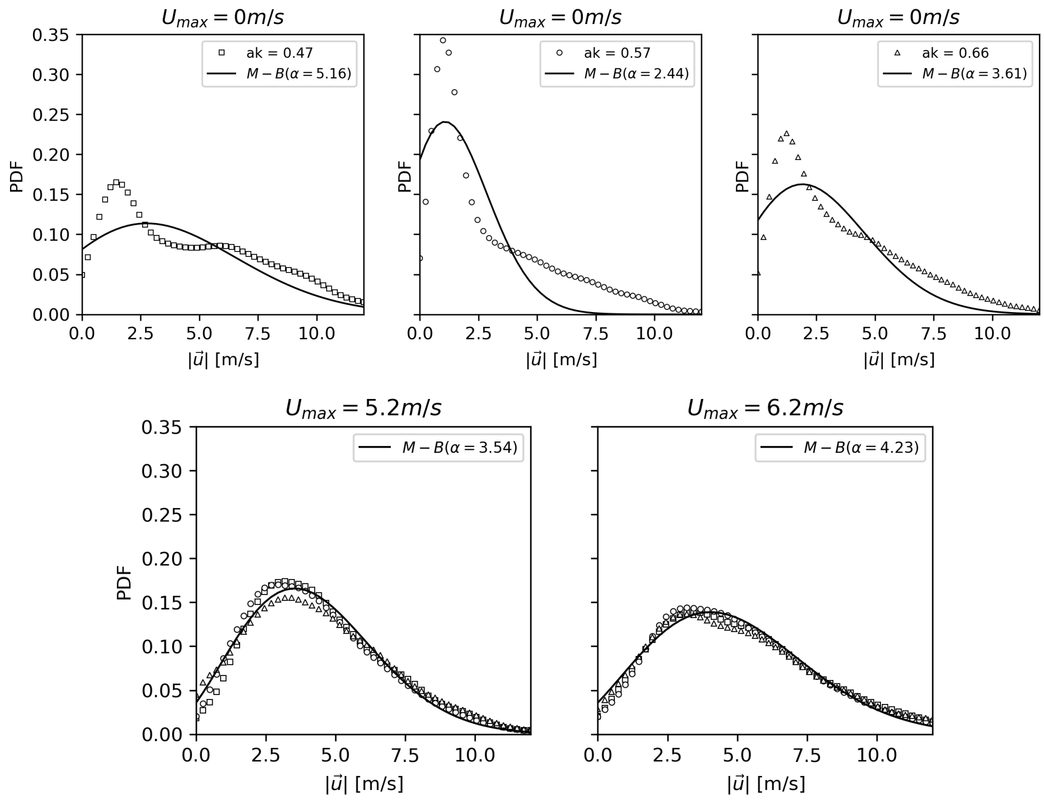

Figure 14. Probability distribution for the speed for the different wind cases.

a Gaussian distribution, but only for $U_{max} = 6.2\,\mathrm{ms^{-1}}$ the data resembles closely the distribution suggested by La Porta et al. (2001) where the extreme cases have the largest probability. We can point out that the values of the normalized acceleration are not as high as the presented in the mentioned article. This can be related to the values of Re_λ, which were calculated to be $Re_\lambda \leq 310$. In the case of La Porta et al. (2001) $Re_\lambda \geq 200$. The low wind speeds used for this work can be the reason why the turbulent tail of the accelerations was not so pronounced. Nonetheless, we can confirm that the dynamics of the initial droplet distribution is affected by the presence of wind even from velocities as low as $5\,\mathrm{ms^{-1}}$. The study of these distributions contributes to the understanding of the complex phenomena that occur at the ocean surface.

4 Conclusions

The initial distribution of droplets after a wave breaking event has been studied for droplets between $0.3\,\mathrm{mm} \leq D_e \leq 11\,\mathrm{mm}$. The influence of wind on this initial distributions has been addressed by comparing cases without wind and low wind velocities. The analysis shows that the distribution of droplets has the same shape in all cases and it is in agreement to the Probability Distribution Function presented in previous studies. A shift of the mean diameter is found and correlated to the energy content of the breaking wave which could point out to a relation between the wave energy and the volume of the mean ligament created during breaking.

As for the velocities and accelerations, the distributions show noticeable differences between the cases without wind and the cases with wind. The presence of wind creates a turbulent flow that affect the movement of the droplets from its separation of the liq-

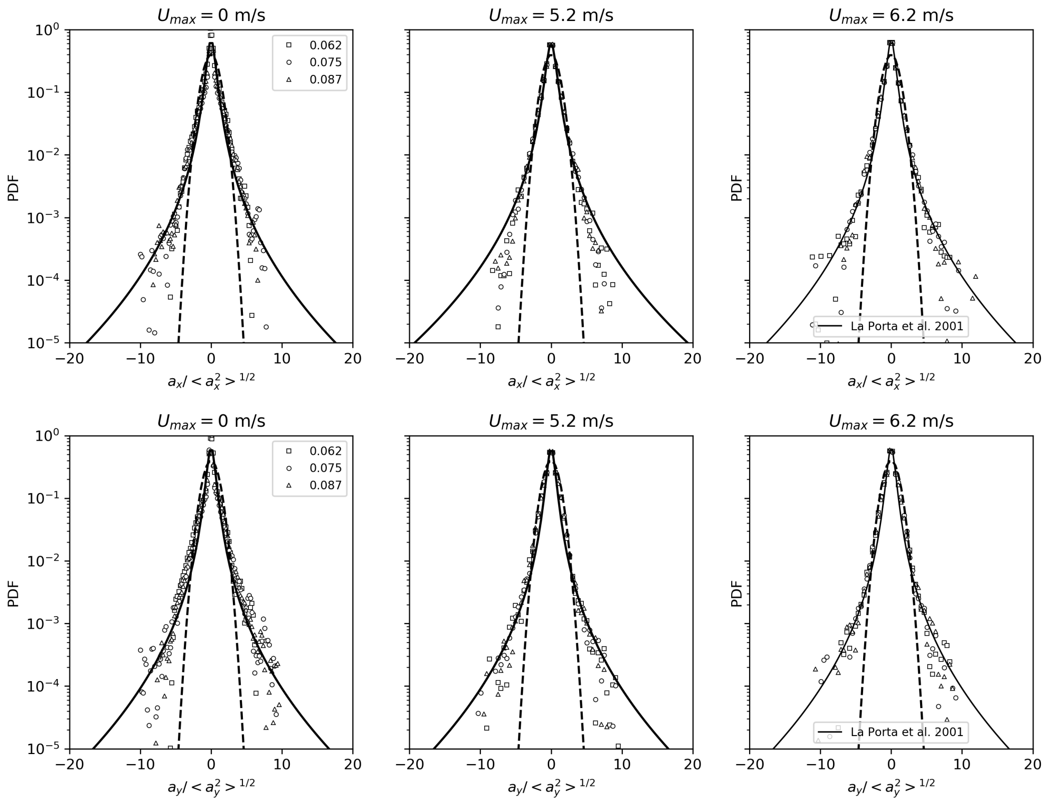

Figure 15. Probability distribution for the acceleration components for the different wind cases. Maximum values of Re_λ are $Re_{\lambda,0} = 42$, $Re_{\lambda,5.2} = 280$ and $Re_{\lambda,6.2} = 310$; where the subscript refers to the correspondent U_{max}

uid bulk. When there is wind, the velocity components are normal distributed and the speed follows the *M-B* distribution as predicted by the theory of statistics in turbulent flows. On the other hand, the velocity components differs from the Gaussian shape when there is no wind, specially the speed has a very distinct shape from the *M-B* distribution and larger probability for extreme values. The findings are similar for the acceleration components where the distribution for larger wind velocity has a more extended exponential tail.

Over all we have a shown that the initial size distribution of droplets is subjected to the properties of the breaker before and during the breaking. The different mechanisms of droplet generation need to be further studied individually and collectively, as in the nature these mechanisms are always combined and rarely isolated from each other.We have also shown that turbulent dynamics is present since the formation of the droplets, the influence of turbulence in the droplets trajectories will affect their residence times, vertical reach and coalescence, as shown in previous SSGF proposed. But the role of the large droplets is yet to be understood. The presented results and other recent research show that there is a larger amount of large droplets than predicted by previous studies. It is the largest droplets that can more easily breakup and generate more droplets when considering time evolution or increasing wind conditions. Therefore, their presence in the early stages of wave breaking and spray formation needs to be further studied.

Acknowledgments

Funding from the Norwegian Research Council through the project Rigspray (grant number 256435) is gratefully acknowledged. The authors will also like to acknowledge Alex Liberzon and the OpenPTV Software Consortium for the help with the use of OpenPTV. The help of Olav Gundersen in the experimental setup is gratefully acknowledge.

References

Andreas, E. L., Jones, K. F., & Fairall, C. W. (2010). Production velocity of sea spray droplets. *Journal of Geophysical Research: Oceans*, *115*(C12).

Bodaghkhani, A., Dehghani, S.-R., Muzychka, Y. S., & Colbourne, B. (2016). Understanding spray cloud formation by wave impact on marine objects. *Cold Regions Science and Technology*, *129*, 114–136.

Borisenkov, Y. P., & Pchelko, I. (1975). *Indicators for forecasting ship icing* (Tech. Rep.).

Brown, M. G., & Jensen, A. (2001). Experiments on focusing unidirectional water waves. *Journal of Geophysical Research: Oceans*, *106*(C8), 16917–16928.

Clift, R., Grace, J. R., & Weber, M. E. (2005). *Bubbles, drops, and particles.* Courier Corporation.

Consortium, O., et al. (2012). Openptv: Open source particle tracking velocimetry. *2012.,()*.

Crowe, C. T., Schwarzkopf, J. D., Sommerfeld, M., & Tsuji, Y. (2011). *Multiphase flows with droplets and particles.* CRC press.

Dalziel, S. (2017). *Digiflow user guide, dalziel research partners.*

Dehghani, S., Muzychka, Y., & Naterer, G. (2016). Droplet trajectories of wave-impact sea spray on a marine vessel. *Cold Regions Science and Technology*, *127*, 1–9.

Dehghani, S., Naterer, G., & Muzychka, Y. (2016). Droplet size and velocity distributions of wave-impact sea spray over a marine vessel. *Cold Regions Science and Technology*, *132*, 60–67.

Fairall, C., Banner, M., Peirson, W., Asher, W., & Morison, R. (2009). Investigation of the physical scaling of sea spray spume droplet production. *Journal of Geophysical Research: Oceans*, *114*(C10).

Kim, J.-T., & Chamorro, L. P. (2019). Lagrangian description of the unsteady flow induced by a single pulse of a jellyfish. *Physical Review Fluids*, *4*(6), 064605.

La Porta, A., Voth, G. A., Crawford, A. M., Alexander, J., & Bodenschatz, E. (2001). Fluid particle accelerations in fully developed turbulence. *Nature*, *409*(6823), 1017–1019.

Mordant, N., Crawford, A. M., & Bodenschatz, E. (2004). Experimental lagrangian acceleration probability density function measurement. *Physica D: Nonlinear Phenomena*, *193*(1-4), 245–251.

Mueller, J. A., & Veron, F. (2009). A sea state–dependent spume generation function. *Journal of physical oceanography*, *39*(9), 2363–2372.

Ortiz-Suslow, D. G., Haus, B. K., Mehta, S., & Laxague, N. J. (2016). Sea spray generation in very high winds. *Journal of the Atmospheric Sciences*, *73*(10), 3975–3995.

Pope, S. (1994). Lagrangian pdf methods for turbulent flows. *Annual review of fluid mechanics*, *26*(1), 23–63.

Ryerson, C. C. (1990). Atmospheric icing rates with elevation on northern new england mountains, usa. *Arctic and Alpine Research*, *22*(1), 90–97.

Shnapp, R., Shapira, E., Peri, D., Bohbot-Raviv, Y., Fattal, E., & Liberzon, A. (2019). Extended 3d-ptv for direct measurements of lagrangian statistics of canopy turbulence in a wind tunnel. *Scientific reports*, *9*(1), 1–13.

Stokes, M., Deane, G., Prather, K., Bertram, T., Ruppel, M., Ryder, O., . . . Zhao, D. (2013). A marine aerosol reference tank system as a breaking wave analogue for the production of foam and sea-spray aerosols. *Atmospheric Measurement Techniques*, *6*(4), 1085.

Veron, F. (2015). Ocean spray. *Annual Review of Fluid Mechanics*, *47*, 507–538.

Veron, F., Hopkins, C., Harrison, E., & Mueller, J. (2012). Sea spray spume droplet production in high wind speeds. *Geophysical Research Letters*, *39*(16).

Villermaux, E., Marmottant, P., & Duplat, J. (2004). Ligament-mediated spray formation. *Physical review letters*, *92*(7), 074501.

Voth, G. A., La Porta, A., Crawford, A. M., Bodenschatz, E., & Alexander, J. (2001). Measurement of particle accelerations in fully developed turbulence. *arXiv preprint physics/0110027*.